A framework proposal for new multiaxial fatigue damage and extreme response spectra in random vibrations frequency analysis

M. Aimé, A. Banvillet, L. Khalij, E. Pagnacco, E. Chatelet, Régis Dufour

▶ To cite this version:

M. Aimé, A. Banvillet, L. Khalij, E. Pagnacco, E. Chatelet, et al.. A framework proposal for new multiaxial fatigue damage and extreme response spectra in random vibrations frequency analysis. Mechanical Systems and Signal Processing, 2024, 213, pp.111338. ⟨10.1016/j.ymssp.2024.111338⟩. ⟨hal-04530289⟩

HAL Id: hal-04530289
https://hal.science/hal-04530289v1

Submitted on 8 Nov 2024

Mechanical Systems and Signal Processing 213 (2024) 111338

Contents lists available at ScienceDirect

Mechanical Systems and Signal Processing

journal homepage: www.elsevier.com/locate/ymssp

A framework proposal for new multiaxial fatigue damage and extreme response spectra in random vibrations frequency analysis

M. Aimé [a,*], A. Banvillet [a], L. Khalij [b], E. Pagnacco [b], E. Chatelet [c], R. Dufour [c]

[a] *CEA DAM, Centre d'Études Scientifiques et Techniques d'Aquitaine (CESTA), 33114 Le Barp, France*
[b] *INSA Rouen Normandie, Laboratory of Mechanics of Normandy (LMN), Normandie université, 76000 Rouen, France*
[c] *Univ Lyon, INSA-Lyon, CNRS UMR5259, LaMCoS, 69621 Villeurbanne, France*

ARTICLE INFO

Communicated by J. Slavič

Keywords:
Gaussian random vibration
Spectral methods
Correlation
Modal proximity
Test tailoring
Modified Wöhler Curve Method
Lemaitre equivalent criterion

ABSTRACT

Fatigue Damage Spectra (FDS) and Extreme Response Spectra (ERS) are well-established tools for characterizing and evaluating the impact of vibration loads on mechanical structures. While this is particularly valuable in producing test-tailored specifications, their current application is limited to uniaxial analysis despite evidence indicating their inadequacy in representing real-world loads, which are often multiaxial.

The proposed method offers a system-oriented approach to characterize and compare multiaxial environments in terms of their severity, independently or not of any physical structure. In addition, it introduces a generalization of the FDS and ERS, referred to as Fatigue Damage multi-Spectrum (FDmS) and Extreme Response multi-Spectrum (ERmS) respectively. These extensions allows for the consideration of multiaxial phenomena, such as correlation and modal proximity. Finally, this paper demonstrates through several case studies the method's capability to capture phenomena not addressed by established uniaxial approaches.

1. Introduction

Many mechanical systems are exposed to random vibrations caused by their operational environment, such as propulsion systems or aerodynamic perturbations. Therefore, accurately characterizing and assessing the severity of these loads is crucial for ensuring component durability and evaluating performance.

The methods developed for this purpose operate either in the time domain – using recorded data – or in the frequency domain, often preferred for its efficiency and ability to preserve the signal's randomness [1–3]. In the frequency domain, measured field data are converted into Power Spectral Densities (PSDs). These PSDs are then analyzed through statistical models that are based on the assumption of a zero-mean Gaussian signal. As a result, the procedure presented in this work applies exclusively to zero-mean stationary Gaussian vibrations.

Fatigue Damage Spectra (FDS) and Extreme Response Spectra (ERS) offer a representation of the random vibrations severity, which eases the comparison between loads and the identification of the most energetic frequencies [4]. They are often used to develop test-tailored specifications by synthesizing mechanical environments into a single equivalent vibration, which simplifies and speeds up the product durability testing [5–8]. Even though FDSs and ERSs can be computed in both the time and frequency domains, they are mainly used in the latter due to its computational efficiency.

---

[*] Corresponding author.
E-mail address: mattias.aime@cea.fr (M. Aimé).

https://doi.org/10.1016/j.ymssp.2024.111338
Received 8 September 2023; Received in revised form 7 March 2024; Accepted 10 March 2024

List of Symbols

C	S-N curve constant
C_{eq}	Multiaxial S-N curve constant
K	Stress–strain elastic coefficient
T	Duration of signal
$\Gamma(\bullet)$	Gamma function
Φ_x	PSD of signal x
$\Phi_{s,eq}$	Equivalent stress response PSD
Φ_{xy}	CSD of signals x and y
$\ddot{r}_{rms}$	RMS acceleration response of the structure
$\mathbf{H_a}$	Accelerance FRF Matrix
$\mathbf{H_r}$	Receptance FRF Matrix
$\mathbf{K}$	Stress–strain elastic coefficients matrix
$\mathbf{Q}$	Equivalent stress coefficients matrix
$\mathbf{\Phi_a}$	Acceleration PSD matrix of the structure's response
$\mathbf{\Phi_e}$	Acceleration PSD matrix of the load
$\mathbf{\Phi_{\ddot{r},eq}}$	Equivalent acceleration PSD of the structure's response
CSD	Cross-Spectral Density
ERS_{std}	Enveloped extreme response spectrum
ERmS	Extreme response multi-spectrum
FDS_{std}	Fatigue damage spectrum for sequential tests
FDmS	Fatigue damage multi-spectrum
FRF	Frequency Response Function
PSD	Power Spectral Density
RMS	Root Mean Square
S – N	Stress - Number of cycles
SDOF	Single Degree of Freedom
τ	Time delay
ξ	Damping
b	Slope of S-N curve
b_{eq}	Multiaxial S-N curve slope
f	Frequency
f_0	Natural frequency
j	Imaginary Unit
r_{RMS}	RMS displacement response of the structure
s_{RMS}	RMS stress

However, the current FDS and ERS are limited to uniaxial applications, while real-life environments can be multiaxial. Moreover, recent research has emphasized the relevance of multiaxial testing, which is seen as more realistic and severe than uniaxial testing [9–11]. The originality of this work is to address this limitation by developing a generalized FDS and ERS, respectively called Fatigue Damage multi-Spectrum (FDmS) and Extreme Response multi-Spectrum (ERmS), which are suited for combined loads. These new spectra can be used in the same way as the original FDS and ERS while simplifying the characterization of real-life environments. They also aim to develop more accurate tailored tests that closely resemble real-world system operating conditions.

Due to its multi-disciplinary nature, this work presents the basics involved in the development of fatigue damage and extreme response multi-spectra, followed by their application in various numerical case studies of increasing realism. These applications are conducted using the Python language with the *Matplotlib*, *Numpy* and *Scipy* packages.

2. Theoretical background

2.1. Characterization of signal properties

2.1.1. Random stationary Gaussian processes

A signal is considered random when its time evolution is neither known nor predictable. Its random nature makes each sample of duration T unique, and their ensemble forms a random process. (Fig. 1-*a*).

The analysis of a long-duration signal is often preceded by a stationary evaluation to ensure that results are independent of the chosen sample. Usually, the stationarity of a process $x(t)$ is evaluated using the ensemble of its samples $x_{i\in[0;N]}(t)$. However, in most cases, only one sample $x_0(t)$ is available. In this scenario, the analysis involves the auto-correlation function R_{xx} of the single sample $x_0(t)$ and its time-delayed counterpart $x_0(t+\tau)$ [12,13] :

$$\mathrm{R}_{xx}(\tau) = \int_{-\infty}^{+\infty} x_0(t)\cdot x_0(t+\tau)\,\mathrm{d}t \tag{1}$$

The process $x(t)$ is then said stationary if its mean value and auto-correlation R_{xx} are both time-independent. However, this is a strong assumption since real-life loads are rarely stationary. A theoretically non-stationary process can still be considered as weakly-stationary if it can be partitioned into stationary intervals.

Finally, a process $x(t)$ is said to be random Gaussian if the set of each samples' instantaneous values follows a Gaussian distribution of mean value μ and standard deviation σ (Fig. 1-*b*). Its probability density at time t is denoted as $\mathrm{p}[x(t)]$ and its expression is:

$$\mathrm{p}\big[x(t)\big] = \frac{1}{\sigma\sqrt{2\pi}}\cdot\exp\left(-\frac{|x(t)-\mu|^2}{2\sigma^2}\right) \tag{2}$$

The time domain offers the ability to process any type of signal, although it tends to be computationally slow. To overcome this drawback, fatigue assessment often employs frequency-domain signal processing, which offers faster computation but is limited to stationary zero-mean Gaussian signals.

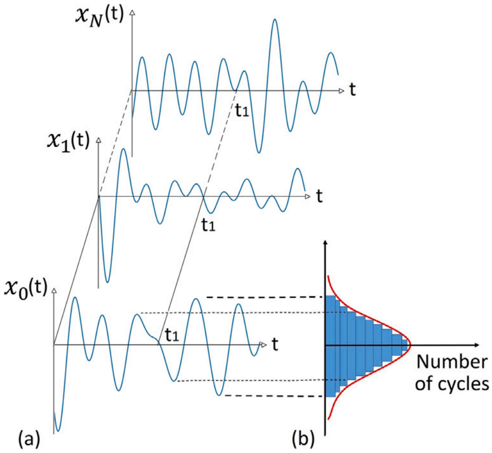

Fig. 1. Samples of a Gaussian random process.

2.1.2. Frequency-domain analysis

A power spectral density (PSD) describes the signal's power distribution in terms of frequencies. One of the main benefits of this description is its capability to preserve the randomness of recorded data. Indeed, an infinite number of energetically equivalent vibrations can be generated with a single PSD, whereas time-domain signals are deterministic. The computation of a one-sided PSD relies on the Fourier transform TF[.] of the zero-mean signal's auto-correlation function R_{xx} (Eq. (1)) [12]:

$$\Phi_x(f) = \mathrm{TF}[\mathrm{R}_{xx}(\tau)] = \int_0^{+\infty} \mathrm{R}_{xx}(\tau) \cdot e^{-j \cdot 2\pi \cdot f \cdot \tau}\ \mathrm{d}\tau \tag{3}$$

When two signals $x(t)$ and $y(t)$ are processed together, it is possible to assess their Cross-Spectral Density (CSD) (Eq. (5)). This spectrum describes the cross-correlation – or the "relationship" – between the two datasets in terms of coherence and phase shift. The CSD definition is based on the inter-correlation function [14]:

$$\mathrm{R}_{xy}(\tau) = \int_{-\infty}^{+\infty} x(t) \cdot y(t+\tau)\ \mathrm{d}t \tag{4}$$

$$\Phi_{xy}(f) = \int_0^{+\infty} \mathrm{R}_{xy}(\tau) \cdot e^{-j \cdot 2\pi \cdot f \cdot \tau}\ \mathrm{d}\tau \tag{5}$$

A CSD Φ_{xy} can also be defined from the related PSDs Φ_x and Φ_y by introducing a correlation coefficient (Eq. (6)). It is a complex number with a modulus ρ, which provides information about the signals' coherence (their "similarities"), and a phase angle φ representing the phase-shift between the data sets. Usually, CSDs are therefore complex functions [13].

$$\Phi_{xy}(f) = \sqrt{\Phi_x(f) \cdot \Phi_y(f)} \cdot \rho_{xy}(f) \cdot e^{\ j \cdot \varphi_{xy}(f)} \tag{6}$$

The spectral analysis of a random vibrations from their PSDs usually requires the evaluation of spectral moments [14,15] as they provide information about the dataset's properties. The ith spectral moment m_i of a stationary random signal described by a PSD Φ is computed as follows:

$$m_i(\Phi) = \int_0^{+\infty} (2\pi f)^i \cdot \Phi(f) \quad \mathrm{d}f \tag{7}$$

These spectral moments are especially used to assess the frequency of positive slope zero crossings per time unit, written n_0^+ [16]:

$$n_0^+ = \frac{1}{2\pi} \cdot \sqrt{\frac{m_2}{m_0}} \tag{8}$$

as well as the expected positive peak frequency per time unit n_p^+:

$$n_p^+ = \frac{1}{2\pi} \cdot \sqrt{\frac{m_4}{m_2}} \tag{9}$$

The computation of Eq. (8) and/or Eq. (9) is usually required to perform fatigue damage analysis since these numbers provide information about the number of cycles, as will be further discussed.

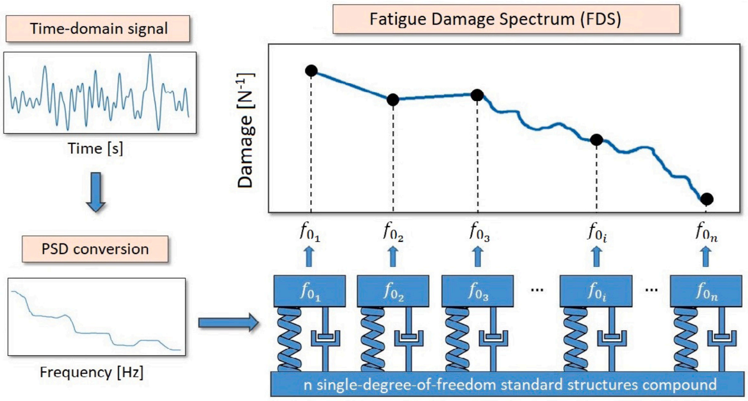

Fig. 2. Process for generating fatigue damage spectra.

2.2. Fatigue damage spectrum (FDS)

The fatigue damage spectrum (FDS) provides a representation of the expected damage caused by random vibrations on a single degree-of-freedom (SDOF) structure, depending on its resonant frequency (Fig. 2).It is important to note that the purpose of this spectrum is neither to precisely describe the damage caused to a structure nor its lifetime. Instead, it provides a general understanding of the actual load severity based on standardized data and a reference structure. It is thus used for system-scale comparative studies, such as comparing the potential damage of different vibrations or identifying the most vulnerable components in a system.

The process of building fatigue damage spectra involves several steps, beginning with the computation of the stress response PSD Φ_s of the SDOF reference structure. For linear systems, the magnitude of the receptance frequency response function (FRF) $|H_a|$ which relates the acceleration of the load $\ddot{x}(t)$ to the relative displacement response $r(t)$ is defined as follows:

$$|H_a(f)| = \frac{1}{(2\pi f_0)^2} \cdot \frac{1}{\sqrt{4\xi^2(f/f_0)^2 + \left[1-(f/f_0)^2\right]^2}} \tag{10}$$

The receptance FRF H_a is fully determined by the resonant frequency f_0 and damping coefficient ξ of the SDOF system, typically set at 5% [4,15]. This value, although arbitrary, must be maintained consistent throughout the analysis in order to ensure that comparisons between spectra remain meaningful.

The SDOF stress response PSD Φ_s can then be computed from the receptance FRF (Eq. (10)) and the load PSD $\Phi_{\ddot{x}}$ [14]. An elastic coefficient K is introduced in accordance with the assumption of linearity.

$$\Phi_s(f) = K^2 \cdot \Phi_r(f) = K^2 \cdot |H_a(f)|^2 \cdot \Phi_{\ddot{x}}(f) \tag{11}$$

An arbitrary elastic coefficient value $K = 1$ is usually assumed when no real material is considered [4]. Then, a second step aims to estimate the damage of the reference structure from the parameter n_0^+ (Eq. (8)) and the RMS stress s_{RMS}, which is defined as follows:

$$s_{RMS}^2 = m_0(\Phi_s) = \int_0^{+\infty} \Phi_s \, \mathrm{d}f \tag{12}$$

The number of cycles to failure N_r, computed from the RMS stress (Eq. (12)), can be estimated using the *S-N* relation (Eq. (13)) and its coefficients b and C [17]. Similar to the elastic coefficient K and the damping coefficient ξ, the parameters of the *S-N* curve are set to standard values when no real material is considered (or a material with unknown properties). A fatigue exponent $b = 8$ is commonly used for structural materials, and the fatigue constant C is usually set to a unit value [4]. In fact, the *S-N* curve coefficients b and C often represent system-equivalent parameters since the structure may be an assembly of several components made from various materials.

$$N_r \cdot s_{RMS}^b = C \tag{13}$$

While various spectral methods are available [18], the conventional approach for computing (FDSs) typically involves the assessment of the damage induced by a load applied over a duration T under the Narrow-Band approximation (Eq. (14)). This method is favored due to its established conservatism across a wide range of process bandwidths [19], making it especially advantageous for the development of specifications in vibration durability testing.

$$\mathrm{FDS}_{NB} = n_0^+ \cdot T \cdot \frac{2^{b/2}}{C} \cdot s_{RMS}^b \cdot \Gamma\left(1 + \frac{b}{2}\right) \tag{14}$$

The Narrow-band expression relies on the Gamma function Γ as well as the Palmgren-Miner linear cumulative damage rule (Eq. (15)) [20]. It gives an estimation of the total fatigue damage D due to $n_{i\in[1;N]}$ cycles of N vibrations at stress levels that would cause failure at $N_{r_{i\in[1;N]}}$ cycles (Eq. (15)).

$$D = \sum_{i=1}^{N} \frac{n_i}{N_{r_i}} \tag{15}$$

As no universally accepted cumulative damage law exists, the Palmgren-Miner rule is still widely used due to its simplicity, despite its potential inaccuracy in some cases [21,22].

The computation of the fatigue damage (Eq. (14)) for various resonant frequencies of the SDOF structure generates the FDS related to the analyzed random load (Fig. 2). This spectrum simplifies the comparison of damage severity caused by different loads based on the structure's resonant frequency. The FDS can also identify the frequencies where the estimated damage is especially significant and, as a result, highlight the most vulnerable components of the system.

Since the reference SDOF structure is uniaxial, it only account for unidirectional loads. As a result, the FDS cannot be used for multiaxial load analysis, even though this type of environments is more representative of real-life operational loads.

Most vibration tests use an axis-by-axis approach where each component of the multiaxial load is applied successively on the respective axis of the structure, as described in various standards [4,23–25]. Because of the uniaxial nature of fatigue damage spectra, the procedure must be repeated for each load component to obtain a separate FDS for each excitation axis. By hypothesis, the damage caused by the sequentially-applied uniaxial loads are assumed to be equivalent to the damage generated by the multiaxial one. The multi-directional damage caused by N sequentially-applied components of the load, noted FDS_{std}, can be estimated as follows (the subscript *std* stands for "standard"):

$$\mathrm{FDS}_{std}(f_{0_1}, \dots, f_{0_N}) = \sum_{i=1}^{N} \mathrm{FDS}_{NB,\mathrm{axis}\ i}(f_{0_i}) \tag{16}$$

Here, $\mathrm{FDS}_{NB,\mathrm{axis}\ i}$ represents the ith axis FDS derived from the Narrow-band approximation (Eq. (14)) and associated with the natural frequency f_{0_i} of that specific axis. The multi-directional standard FDS, denoted as FDS_{std}, is the cumulative result of all single-axis FDS. Therefore, FDS_{std} is a function of all the axes' natural frequencies, explaining the notation $\mathrm{FDS}_{std}(f_{0_1}, \dots, f_{0_N})$.

Yet, by assuming a linear relationship between damage and excitation level, Eq. (16) represents a substantial simplification, given that the actual relationship is rather exponential, as shown in Eq. (41). Moreover, this formulation overlooks the potential impact of cross-axis interaction, which can be significant on the structure's failure time [26–30]. Some of these phenomena will be further investigated in the upcoming case studies (Section 4).

2.3. Extreme response spectrum (ERS)

The Extreme Response Spectrum (ERS) operates on the same principle as the FDS, which is illustrated in Fig. 2. However, instead of offering an estimated damage, it emphasizes the most likely acceleration peak response of the reference SDOF structure [15].

As for the FDS, it is mainly used to compare load severity or to highlight the weak spots of a composite system presenting various resonant frequencies.

The mathematical description of the ERS is based on the Extreme Values Theory. Since the load is presumed Gaussian, the SDOF response can also be stated as such [15]. At first, the RMS value of the relative displacement response r_{RMS} is defined from the frequency of positive slope a-level crossings:

$$N_a^+ = n_0^+ \cdot T \cdot \exp\left(-\frac{a^2}{2r_{RMS}^2}\right) \tag{17}$$

The maximum peak value r_{max} of the response is, by definition, exceeded only once throughout the duration T of the signal. By using Eq. (17), the value $a = r_{max}$ where $N_a^+ = 1$ gives the estimated maximum peak:

$$r_{max} = r_{RMS} \cdot \sqrt{2\log(n_0^+ T)} \tag{18}$$

For linear systems, stress is related to the response through a linear coefficient with $s_{RMS} = K \cdot r_{RMS}$. However, the ERS is defined to compute the extreme response of the reference SDOF structure in terms of acceleration instead of displacement, as estimated by Eq. (18). The ERS can finally be obtained by multiplying the expected maximum peak r_{max} by the quantity $(2\pi \cdot f_0)^2$:

$$\mathrm{ERS}(f_0) = \frac{(2\pi f_0)^2}{K} \cdot s_{RMS} \cdot \sqrt{2\log(n_0^+ T)} \tag{19}$$

ERSs can be expressed directly from the acceleration response PSD using the receptance FRF (Eq. (20)), but it is often more efficient to compute both ERS and FDS from the same stress response PSD s_{RMS} (Eq. (19)) instead of computing two separate ones from different FRF.

$$\mathrm{ERS}(f_0) = \ddot{r}_{RMS} \cdot \sqrt{2\log(n_0^+ T)} \tag{20}$$

As ERSs are primarily designed for uniaxial applications, they require adjustments when dealing with multiple axes. The commonly employed and standardized approach involves generating individual ERSs for each axis of interest, following a procedure similar to that of FDS. Subsequently, an envelope spectrum is created by superimposing these individual spectra, as outlined in the Ref. [4]. This method assumes that the envelope accurately represents the system's response under multiaxial conditions. The resulting extreme response caused by the enveloped ERS of the load's axial components ERS_{std}, can be estimated as follows (where the subscript std refers to "standard"):

$$\mathrm{ERS}_{std}(f_{0_1},\ldots,f_{0_N}) = \max\left[\,\mathrm{ERS}_{\mathrm{axis}\ 1}(f_{0_1}),\ldots,\mathrm{ERS}_{\mathrm{axis}\ N}(f_{0_N})\,\right] \tag{21}$$

Yet, just like the FDS, this solution is only partial as it ignores the possibility of cross-axis interactions and thus may not accurately reflect the severity of real-life environments. It is nonetheless expected that the multiaxiality of the load will have a greater impact on the FDS than on the ERS because of the exponential relationship between load and damage in the FDS (Eq. (14)).

3. Generalized framework for multiaxial loads

Aiming to correct some limitations of the commonly-used uniaxial procedures already described (Sections 2.2 and 2.3), two spectral methods are proposed to assess the fatigue damage and the extreme response of structures subject to combined random loads. These new methods are based on FDSs and ERSs, and are respectively called fatigue damage multi-spectrum (FDmS) and extreme response multi-spectrum (ERmS).

3.1. Assumptions and hypothesis

The FDmS and ERmS share most of the assumptions required for the development of FDS and ERS. Therefore, although this aspect is often implied in uniaxial procedures, this generalized approach also considers a system-scale description, where loads are defined in terms of both translations and rotations. This means that the analysis focuses on characterizing the loads themselves rather than the actual stress state of the structure.

In the case of multiaxial loads, it is assumed that the stress induced by each axial component of the load is exclusively uniaxial along its respective axis. In other words, each translation introduces a distinct uniaxial normal stress on the structure, while each rotation results in a unique uniaxial shear stress. The advantage of this approach is that the analysis can take into account up to six degrees of freedom : three translations and as many rotations. As a result, the structure is defined by six resonant frequencies, as only the first mode of each axis is considered. It is assumed that other natural frequencies are smaller contributors to the response and can be neglected. However, the procedure can account for secondary resonant frequencies if necessary by modifying the FRF definition (Eq. (10)).

3.1.1. Equivalent stress PSD

As previously stated, the reference SDOF structure used in the FDS and ERS procedures has evolved into a multi-degrees-of-freedom (MDOF) system where each load axis generates stresses on the same axis. This requires the development of a uniaxial stress-state equivalent PSD, as damage assessment requires a scalar, uniaxial stress. To this end, a 6 × 6 PSD matrix is introduced to depict the multiaxial stress state of the reference MDOF structure. This matrix can be derived from the excitation PSD matrix $\mathbf{\Phi_e}$, the diagonal-assumed matrix of the structure's receptance FRF $\mathbf{H_r}$ and the diagonal matrix of the elastic coefficients $\mathbf{K}$:

$$\mathbf{\Phi_s} = \mathbf{K}\cdot\mathbf{H_r}\cdot\mathbf{\Phi_e}\cdot\mathbf{H_r^H}\cdot\mathbf{K}^{\mathrm{T}} \tag{22}$$

where $\mathbf{H_r^H}$ is the conjugated and transposed terms matrix of $\mathbf{H_r}$, and $\mathbf{K}^{\mathrm{T}}$ is the transposed matrix of $\mathbf{K}$. In addition, the symmetrical matrix of the load's acceleration PSD $\mathbf{\Phi_e}$ is defined as follows, where extra-diagonal terms are the loads' cross-correlations PSDs.

$$\mathbf{\Phi_e} = \begin{pmatrix} \boldsymbol{\Phi}_{\ddot{x}} & \boldsymbol{\Phi}_{\ddot{x}\ddot{y}} & \boldsymbol{\Phi}_{\ddot{x}\ddot{z}} & \boldsymbol{\Phi}_{\ddot{x}\ddot{\theta}_x} & \boldsymbol{\Phi}_{\ddot{x}\ddot{\theta}_y} & \boldsymbol{\Phi}_{\ddot{x}\ddot{\theta}_z} \\ & \boldsymbol{\Phi}_{\ddot{y}} & \boldsymbol{\Phi}_{\ddot{y}\ddot{z}} & \boldsymbol{\Phi}_{\ddot{y}\ddot{\theta}_x} & \boldsymbol{\Phi}_{\ddot{y}\ddot{\theta}_y} & \boldsymbol{\Phi}_{\ddot{y}\ddot{\theta}_z} \\ & & \boldsymbol{\Phi}_{\ddot{z}} & \boldsymbol{\Phi}_{\ddot{z}\ddot{\theta}_x} & \boldsymbol{\Phi}_{\ddot{z}\ddot{\theta}_y} & \boldsymbol{\Phi}_{\ddot{z}\ddot{\theta}_z} \\ & & & \boldsymbol{\Phi}_{\ddot{\theta}_x} & \boldsymbol{\Phi}_{\ddot{\theta}_x\ddot{\theta}_y} & \boldsymbol{\Phi}_{\ddot{\theta}_x\ddot{\theta}_z} \\ & \ldots & & & \boldsymbol{\Phi}_{\ddot{\theta}_y} & \boldsymbol{\Phi}_{\ddot{\theta}_y\ddot{\theta}_z} \\ & & & & & \boldsymbol{\Phi}_{\ddot{\theta}_z} \end{pmatrix} \tag{23}$$

For a material-scale analysis, Preumont's Equivalent Von Mises Stress (EVMS) [31,32] is a widely used and accepted method for producing equivalent stress PSD in spectral domain. This is mainly due to its simplicity and relative accuracy [33,34] despite some limitations for certain materials and load configurations [35,36]. Its matrix formulation can be expressed as follows:

$$\boldsymbol{\Phi}_{s,\mathrm{eq}}^{\mathrm{EVMS}} = \mathrm{Trace}\big(\mathbf{Q_{VM}}\cdot\mathbf{\Phi_s}\big) \tag{24}$$

where $\mathbf{Q_{VM}}$ is the Von Mises coefficients matrix:

$$\mathbf{Q_{VM}} = \begin{pmatrix} 1 & -0.5 & -0.5 & 0 & 0 & 0 \\ -0.5 & 1 & -0.5 & 0 & 0 & 0 \\ -0.5 & -0.5 & 1 & 0 & 0 & 0 \\ 0 & 0 & 0 & 3 & 0 & 0 \\ 0 & 0 & 0 & 0 & 3 & 0 \\ 0 & 0 & 0 & 0 & 0 & 3 \end{pmatrix} \tag{25}$$

An alternative to this popular formulation is derived from the Equivalent Lemaitre Stress [37]. It has been introduced in order to incorporate the effect of hydrostatic stress and address some limitations of EVMS. Its matrix expression is similar to the EVMS formulation [38]:

$$\Phi_{s,\mathrm{eq}}^{\mathrm{LM}} = \mathrm{Trace}\left(\mathbf{Q_{LM}} \cdot \mathbf{\Phi_s}\right) \tag{26}$$

where $\mathbf{Q_{LM}}$ is the Lemaitre coefficients matrix:

$$\mathbf{Q_{LM}} = \begin{pmatrix} 1 & -\nu & -\nu & 0 & 0 & 0 \\ -\nu & 1 & -\nu & 0 & 0 & 0 \\ -\nu & -\nu & 1 & 0 & 0 & 0 \\ 0 & 0 & 0 & 2.(1+\nu) & 0 & 0 \\ 0 & 0 & 0 & 0 & 2.(1+\nu) & 0 \\ 0 & 0 & 0 & 0 & 0 & 2.(1+\nu) \end{pmatrix} \tag{27}$$

As can be seen when the Poisson's ratio ν is set to 0.5, the EVMS formulation is identical to the equivalent Lemaitre stress PSD (Eqs. (24) and (26)). In addition, both formulations take account of the multiaxial stress-state and material properties of the structure. However, these properties may still be unknown during the specification development process, since it is usually performed prior to or during the design of the system. Hence, the use of a generic coefficient matrix $\mathbf{Q}$ filled with parameters q_{ij} where $(i,j) \in [1;6]^2$ is suggested. Similarly to parameters K, b, C and ξ, the values assigned to $\mathbf{Q}$ can be standard or adapted to a specific structure if desired, as long as they remain consistent throughout the analysis. As a result, the generic equivalent stress PSD can be expressed in the following manner:

$$\Phi_{s,\mathrm{eq}} = \mathrm{Trace}\left(\mathbf{Q} \cdot \mathbf{K} \cdot \mathbf{H_r} \cdot \mathbf{\Phi_e} \cdot \mathbf{H_r^H} \cdot \mathbf{K}^{\mathrm{T}}\right) \tag{28}$$

For the applications discussed further in Section 4, $\mathbf{Q}$ will use Lemaitre's coefficients with $\nu = 0.3$ (Eq. (27)). This choice aligns with the values of ν commonly encountered in various metallic materials, simplifying result comparisons with experimental observations. It can be deduced from Eq. (27) that both the off-diagonal and last three diagonal terms depend on ν. These coefficients can be regarded as the influence of, respectively, the correlations and the angular loads on the equivalent stress response. Therefore, an increase of ν amplify the weight of correlations and rotation-induced damages.

3.1.2. Equivalent resultant acceleration PSD

The Section 2.3 described how the ERS relies on the acceleration response of the structure for estimating the most probable extreme response. In multiaxial conditions, each axis contributes to the resultant acceleration response $\ddot{r}(t)$. To make full use of the 6-DOF configuration, the response must take into account both linear acceleration responses $\ddot{x}(t), \ddot{y}(t), \ddot{y}(t)$ and angular ones $\ddot{\theta}_x(t), \ddot{\theta}_y(t), \ddot{\theta}_z(t)$. Assuming that point P in polar coordinates $(r, \theta_{0,z})$ is subjected to a z-axis rotation θ_z, centered at O. The position vector $\overrightarrow{OP}$ can be expressed as follows:

$$\overrightarrow{\mathrm{OP}} = r\cos(\theta_0 + \theta_z)\vec{x} + r\sin(\theta_0 + \theta_z)\vec{y} \tag{29}$$

The acceleration resulting from the rotation around the z-axis can thus be defined in the following manner:

$$\frac{\mathrm{d}^2\overrightarrow{\mathrm{OP}}}{\mathrm{d}t^2} = -r\left[\ddot{\theta}_z \cdot \sin(\theta_0 + \theta_z) + \dot{\theta}_z^2 \cdot \cos(\theta_0 + \theta_z)\right]\vec{x} + r\left[\ddot{\theta}_z \cdot \cos(\theta_0 + \theta_z) - \dot{\theta}_z^2 \cdot \sin(\theta_0 + \theta_z)\right]\vec{y} \tag{30}$$

Considering that vibrations result in minor displacements and rotations, it is possible to derive a linear approximation of Eq. (30) based on the initial position $(x_0; y_0)$ of the studied point P:

$$\theta_z \approx 0 \Rightarrow \begin{cases} r\cos(\theta_0 + \theta_z) \approx r\cos(\theta_{0,z}) = x_0 \\ r\sin(\theta_0 + \theta_z) \approx r\sin(\theta_{0,z}) = y_0 \end{cases} \tag{31}$$

It can be inferred from Eq. (30) that for accelerations below $4.f^2$ – where f represents the minimal excitation frequency – neglecting the angular velocity $\dot{\theta}_z$ results in small errors. Specifically, these errors remain under 10% when the magnitudes of the coordinates x_0 and y_0 are roughly equivalent. As a result, by substituting Eq. (31) in Eq. (30) and simplifying the latter by disregarding the angular velocity provides the definition of the Z-axis acceleration (Eq. (32)c).

Following the same approach considering this time three independant rotations θ_x, θ_y and θ_z, the vector of the rotation-induced acceleration can be expressed as:

$$\frac{\mathrm{d}^2\overrightarrow{\mathrm{OP}}}{\mathrm{d}t^2} \approx \begin{cases} -\, z_0\ddot{\theta}_x \cdot \vec{y} \;+\; y_0\ddot{\theta}_x \cdot \vec{z} & \text{(a)} \\ -\, x_0\ddot{\theta}_y \cdot \vec{z} \;+\; z_0\ddot{\theta}_y \cdot \vec{x} & \text{(b)} \\ -\, y_0\ddot{\theta}_z \cdot \vec{x} \;+\; x_0\ddot{\theta}_z \cdot \vec{y} & \text{(c)} \end{cases} \tag{32}$$

Using Eqs. (32)a, (32)b, (32)c, in addition to the linear accelerations $\ddot{x}, \ddot{y}$ and $\ddot{z}$, an approximation for the magnitude of a 6-DOF acceleration can be expressed as follows:

$$\left\|\frac{\mathrm{d}^2\overrightarrow{\mathrm{OP}}}{\mathrm{d}t^2}\right\|^2 = (\ddot{x} + z_0\ddot{\theta}_y - y_0\ddot{\theta}_z)^2 + \;(\ddot{y} + x_0\ddot{\theta}_z - z_0\ddot{\theta}_x)^2 + \;(\ddot{z} + y_0\ddot{\theta}_x - x_0\ddot{\theta}_y)^2 \tag{33}$$

However, it is necessary to rework the time-domain expression presented in Eq. (33) to make it suitable for frequency-domain analysis. Furthermore, similar to the formulation of equivalent stress discussed in Section 3.1.1, the PSD of the resultant acceleration cannot be directly obtained from the time-domain formulation (Eq. (33)), due to non-zero mean and non-Gaussian properties.

The introduction of an acceleration vector defined as $\mathbf{a} = (\ddot{x}, \ddot{y}, \ddot{z}, \ddot{\theta}_x, \ddot{\theta}_y, \ddot{\theta}_z)^{\mathrm{T}}$, leads to a time-domain expression Eq. (33) that can be redefined using a symmetric 6 × 6 matrix $\mathbf{Q_a}$:

$$\left\| \frac{\mathrm{d}^2\overrightarrow{\mathrm{OP}}}{\mathrm{d}t^2} \right\|^2 = \mathbf{a}^{\mathrm{T}} \cdot \mathbf{Q_a} \cdot \mathbf{a} = \mathrm{Trace}(\mathbf{Q_a} \cdot \mathbf{a} \cdot \mathbf{a}^{\mathrm{T}}) \tag{34}$$

The coefficients of $\mathbf{Q_a}$ can be identified by equaling Eqs. (33) and (34):

$$\mathbf{Q_a} = \begin{pmatrix} 1 & 0 & 0 & 0 & z_0 & -y_0 \\ 0 & 1 & 0 & -z_0 & 0 & x_0 \\ 0 & 0 & 1 & y_0 & -x_0 & 0 \\ 0 & -z_0 & y_0 & y_0^2 + z_0^2 & -x_0.y_0 & -x_0.z_0 \\ z_0 & 0 & -x_0 & -x_0.y_0 & x_0^2 + z_0^2 & -y_0.z_0 \\ -y_0 & x_0 & 0 & -x_0.z_0 & -y_0.z_0 & x_0^2 + y_0^2 \end{pmatrix} \tag{35}$$

With a similar approach as Preumont's EVMS demonstration [32,38], using the expectation E[.] of Eq. (34) leads to the introduction of a resultant acceleration equivalent PSD:

$$\boldsymbol{\Phi}_{\ddot{r},\mathrm{eq}} = \mathrm{Trace}(\mathbf{Q_a} \cdot \mathbf{\Phi_a}) \tag{36}$$

This expression allows for the development of a 6-DOF extreme response spectrum in the frequency domain, a topic that will be explored further. Similarly to the equivalent stress formulation, the non-zero off-diagonal parameters of Q_a, show that some CSDs between angular loads will impact the structure's response. In addition, Eq. (35) emphasizes that the influence of each angular PSDs and CSDs on the response depends on the coordinates of the analyzed point $(x_0\,;\,y_0\,;\,z_0)$.

3.1.3. *Multiaxial S-N curve*

When a material is exposed to combined loads, the *S-N* curves for tension and torsion can exhibit differences. Failing to account for this phenomenon in multiaxial load analysis can lead to inaccurate fatigue damage assessment. In 2001, Susmel and Lazzarin introduced the *Modified Wöhler Curve Method* (MWCM), which involve adjusting the *S-N* coefficients *b* and *C* by considering the relative weighting of tension and torsion *S-N* curves [39]. This method has been widely discussed and shown to produce accurate results in both time and frequency domains [35,40,41]. It has also been defined in the frequency-domain using the equivalent Lemaitre stress [38], already described in Eq. (26).

The weighting between the tension and torsion *S-N* curves is assessed from the load multiaxiality, which is expressed by the following variable:

$$\lambda = 3\sqrt{\frac{m_0(\boldsymbol{\Phi}_s^h)}{m_0(\boldsymbol{\Phi}_{s,\mathrm{eq}}^{\mathrm{LM}})}} \tag{37}$$

As described in Eq. (37), λ is computed from the zero-order spectral moment (Eq. (7)) of the equivalent Lemaitre' stress $\boldsymbol{\Phi}_{s,\mathrm{eq}}^{\mathrm{LM}}$ (Eq. (26)) and the hydrostatic stress $\boldsymbol{\Phi}_s^h$:

$$\boldsymbol{\Phi}_s^h = \frac{\boldsymbol{\Phi}_{s_x} + \boldsymbol{\Phi}_{s_y} + \boldsymbol{\Phi}_{s_z}}{9} \tag{38}$$

The FDmS and ERmS approaches assume that pure tension loads are caused exclusively by translations, and pure torsion loads are caused by rotations. Consequently, in line with the principles of the Modified Wöhler Curve Method, variations may occur between the *S-N* curves for rotational and translational loading conditions for a given structure, as illustrated in Fig. 3. Continuing with this analogy, it becomes possible to evaluate the system-equivalent *S-N* curve coefficients b_{eq} and C_{eq} from the translational *S-N* curve coefficients $(b_t\ C_t)$ and their rotational counterpart $(b_r,\ C_r)$. Indeed, as λ varies (Eq. (37)), the multiaxial *S-N* curve approaches either the translational or rotational S-N curve (Eq. (39)). Consequently, a purely rotational load is considered when $\lambda = 0$ and a strictly translational load is related to $\lambda = 1$.

The exponent b_{eq} of the multiaxial system-equivalent *S-N* curve can be defined as:

$$b_{eq} = \lambda \cdot b_t + (1 - \lambda) \cdot b_r \tag{39a}$$

along with the multiaxial S-N curve constant:

$$\log(C_{eq}) = \lambda \cdot \log(C_t) \ + (1 - \lambda) \cdot \log(\sqrt{2(1 + \nu)}^{\,-b_r} \cdot C_r) \tag{39b}$$

The use of these coefficients (Eq. (39)) is a proposal aiming to fine-tune the choice of the *S-N* curve parameters in the absence of identification tests and when standard parameters must be set. However, it is important to note that such tests are recommended for achieving precise estimations. Currently and to the authors' knowledge, no trial has been conducted to assess the differences between the *S-N* curve parameters of a structure exposed to translational or rotational loads. As a result, no value can be recommended for rotational parameters b_r and C_r, unlike the translational ones that follow the uniaxial recommendations ($b_t = b \approx 8$ and $C_t = C \approx 1$).

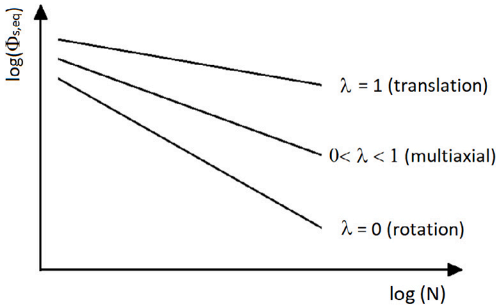

Fig. 3. System-equivalent multiaxial S-N curve.

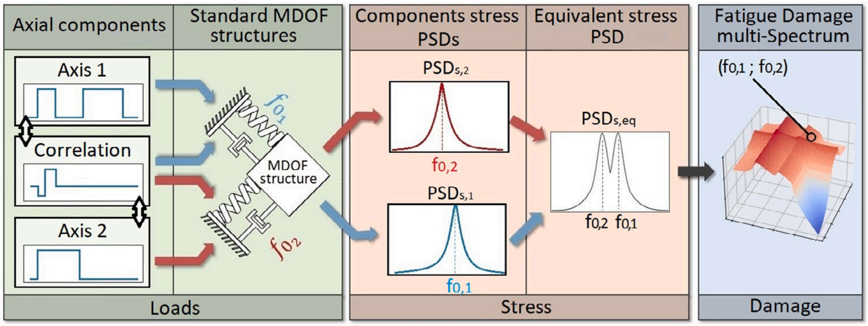

Fig. 4. Process for generating fatigue damage multi-spectra.

3.2. *Fatigue damage multi-spectrum*

The development of a fatigue damage multi-spectrum (FDmS) able to take into account the load multiaxiality requires the implementation of the previously-described MDOF structure, the equivalent stress PSD (Eq. (28)) and eventually the multiaxial *S-N* curve (Eq. (39)). Nevertheless, the outline of the FDmS development procedure remains very similar to the uniaxial one (Fig. 4):

Note that due to the change in the stress computation step, the RMS stress value s_{RMS} is now assessed using the equivalent stress PSD $\Phi_{s,eq}$ (Eq. (28)), which results in the following re-definition of s_{RMS} (Eq. (12)):

$$s_{RMS}^2 = \int_0^{+\infty} \Phi_{s,eq} \, \mathrm{d}f \tag{40}$$

The FDmS relies on a similar expression to the FDS one (Eqs. (14) and (41)) but uses the new definition of s_{RMS} (Eq. (40)). In addition, the terms b and C are substituted by b_{eq} and C_{eq} to reflect the use of a multiaxial system-equivalent *S-N* curve:

$$\mathrm{FDmS}_{NB} = n_0^+ \cdot T \cdot \frac{2^{b_{eq}/2}}{C_{eq}} \cdot s_{RMS}^{b_{eq}} \cdot \Gamma\left(1 + \frac{b_{eq}}{2}\right) \tag{41}$$

Despite the capability of the FDmS procedure to consider up to 6-DOF loads, the applications further discussed are focused on bi- and tri-axis ones because of the difficulty to illustrate higher-dimensional spaces.

3.3. *Extreme response multi-spectrum*

As stated in Section 2.3, the ERS and FDS share the same RMS relative displacement response r_{RMS}. This response relies on the strain–stress coefficient K to compute the stress (Eq. (14)) and the quantity $(2.\pi.f_0)^2$ to compute the acceleration (Eq. (19)). However, this solution is not acceptable for the development of FDmS and ERmS since the quantity $(2.\pi.f_0)^2$ is no longer applicable, given that the resulting response is derived from multiple resonant frequencies. Consequently, the resultant acceleration must be directly computed from the accelerance FRF of each axis. In addition, a frequency-domain formulation that connects the resultant acceleration response $\ddot{r}(t)$ to the load's excitation matrix is introduced with the help of Eq. (36). Indeed, the matrix of the structure's acceleration response PSD $\mathbf{\Phi_a}$ can be substituted from Eq. (36) by using the PSD matrix of the load's accelerations $\mathbf{\Phi_e}$ (Eq. (23)) and the diagonal matrix of the accelerance FRF $\mathbf{H_a}$:

$$\Phi_{\ddot{r},eq} = \mathrm{Trace}(\mathbf{Q_a} \mathbf{H_a} \mathbf{\Phi_e} \mathbf{H_a}^{\mathrm{H}}) \tag{42}$$

where $\mathbf{H_a}^{\mathrm{H}}$ is the transposed and conjugated matrix of $\mathbf{H_a}$.

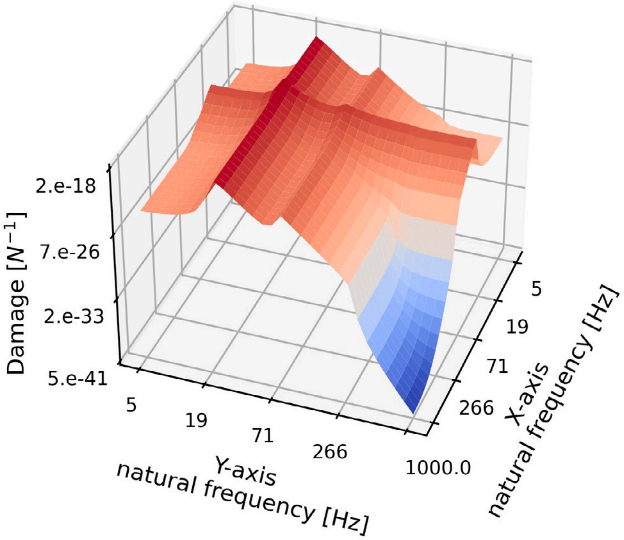

Fig. 5. 3D representation of a biaxial FDmS.

The RMS value of the acceleration response $\ddot{r}_{RMS}$ used in the uniaxial ERS formulation (Eq. (20)) is therefore substituted to the equivalent acceleration response $\ddot{r}_{RMS,eq}$ (Eq. (43)):

$$\ddot{r}_{RMS,eq} = \int_{f_{min}}^{f_{max}} \boldsymbol{\Phi}_{\ddot{r},eq} \,\mathrm{d}f \tag{43}$$

As both $\boldsymbol{\Phi}_{\ddot{r},eq}$ and $\boldsymbol{\Phi}_{\mathbf{e}}$ describe zero-mean stationary Gaussian processes, Eqs. (17) and (18) from the ERS demonstration remain applicable as does the reasoning that leads to Eq. (20). Therefore, drawing an analogy with the derivation of the ERS formulation, the ERmS can be defined as follows:

$$\mathrm{ERmS} = \ddot{r}_{RMS,eq} \cdot \sqrt{2\log(n_0^+ T)} \tag{44}$$

It should be noted that the ERmS relies on the coordinates of the analyzed point due to the inclusion of angular accelerations (Eq. (35)). To address this issue, and alike most other parameters used by the presented procedures, it is possible to use standard values for x_0, y_0 and z_0 as long as they remain consistent throughout the analysis. For instance, a value of $x_0 = y_0 = z_0 = \sqrt{2}/2$ leads to evenly distributed weights between angular and linear accelerations on the resultant.

Another noteworthy observation relates to the substantial contribution of most angular acceleration CSDs in the ERmS whereas they have none in the FDmS (Eqs. (35) and (27)). As a result, it may be relevant to use both procedures in combination to comprehensively describe the excitation load.

4. Numerical case studies: results and discussion

In this section, the proposed procedure is applied to a range of case studies, progressively increasing in complexity, to underscore its capabilities.

4.1. Simple uncorrelated biaxial loading scenario: the effect of multiaxiality

Biaxial environments lead to the creation of a three-dimensional FDmS comprising two frequency dimensions and a third linked to the estimated damage (Fig. 5). This tri-spectrum is computed from the equivalent stress response PSD (Eq. (28)) using the Lemaitre coefficient matrix with $\nu = 0.3$ (Eq. (27)). Additionally, K is set to 1 for each axis, $C = 1$, $b = 8$ and ξ =5%. Given that the loads are uncorrelated, the phase-shift is not defined, and the coherence between the loads is fixed at $\rho_{xy} = 0$.

It is also possible to simulate the damage caused by sequentially-applied loads, as outlined in the standards, using the FDmS method (Section 3.2). This simulation is straightforward since it solely requires adding up the damage multi-spectrum of each load considered one at a time, while disregarding the others (Fig. 6). This comparison can provide useful insights into the estimated damage from both methods.

The relative error between the damage estimated by the standard sequential procedure FDS_{std} (Eq. (16) and Fig. 6) and by the proposed generalized method $FDmS_{NB}$ (Eq. (41) and Fig. 4) is evaluated for each point of the surface using the following equation:

$$\epsilon = 100 \cdot \frac{\mathrm{FDmS}_{NB} - \mathrm{FDS}_{std}}{\mathrm{FDS}_{std}} \tag{45}$$

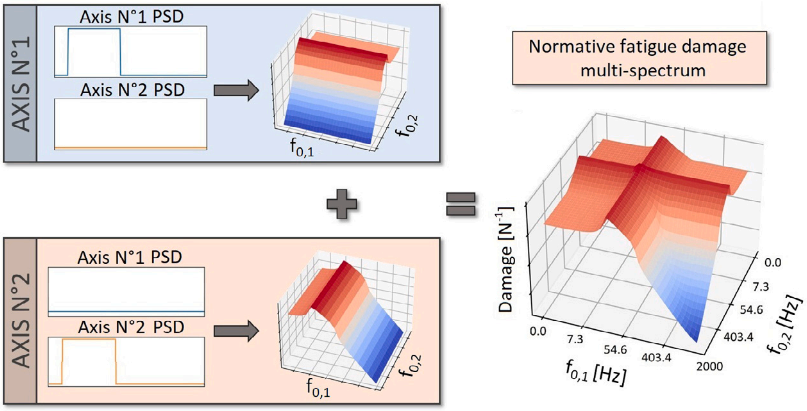

Fig. 6. Method for generating FDmS simulating a sequentially-applied multiaxial load.

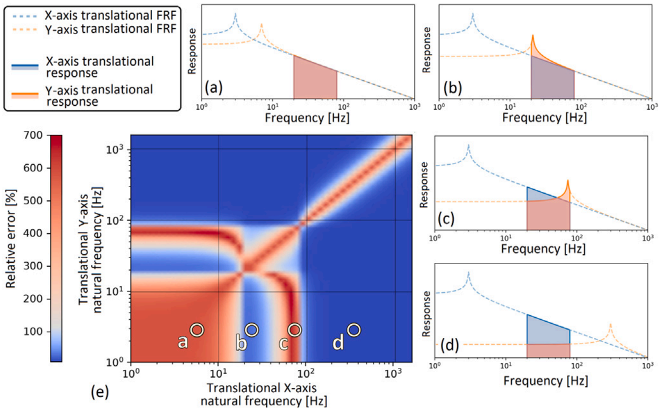

Fig. 7. Relative Fatigue damage error map of standard vs proposed methods - (a) to (d) represent measures of FRF on the map.

For comprehension purpose, the first numerical application is conducted on a simple biaxial environment composed of two uncorrelated translational loads:

$$\begin{aligned} \Phi_{\ddot{x}} = \Phi_{\ddot{y}}(f) &= \begin{cases} 1 & \text{if } f \in [20, 80] \text{ Hz} \\ 0 & \text{else.} \end{cases} \\ \Phi_{\ddot{x}\ddot{y}}(f) &= 0 \end{aligned} \tag{46}$$

The relative error map (Fig. 7-*e*) highlights a close proximity between the estimated damage from the standard sequential method and the proposed multiaxial procedure when the structure's resonant frequencies are widely separated, resulting in a relative error close to zero (blue color). However, the error increases as these frequencies get closer, reaching a maximal ratio of 8 between the two estimations (red color). These results can be inferred from the RMS responses of both axis (Fig. 7-*a* to *d*). By assuming that the damage caused by a biaxial load is equivalent to the sum of two sequentially-applied uniaxial loads (Eq. (16)), the standard method implicitly assumes a linear relationship between damage and load, which is actually exponential.

In this case study, the error between the standard-computed damage and the one estimated by the proposed multiaxial method is consequently directly linked to the error of assuming that the power of a sum is equal to the sum of the powers. Indeed, the ratio between both methods can be expressed as follows from Eqs. (14), (16) and (41):

$$\frac{\mathrm{FDmS_{NB}}}{\mathrm{FDS_{std}}} \approx \frac{n^+_{0,\mathrm{multi}} \cdot (1 + s_{\mathrm{RMS},1}/s_{\mathrm{RMS},1})^{b/2}}{n^+_{0,1} + n^+_{0,2} \cdot (s_{\mathrm{RMS},2}/s_{\mathrm{RMS},1})^{b/2}} \tag{47}$$

where $n^+_{0,\mathrm{multi}}$ is the n^+_0 value of the multiaxial response.

Two potential scenarios arise from Eq. (47) depending on the amplitude ratio between the two axial responses $s_{\mathrm{RMS},1}$ and $s_{\mathrm{RMS},2}$:

1. Both axial responses are very different at a given resonant frequency, causing one to be negligible. As a result, the multiaxial response converges towards a uniaxial one (Fig. 7-*b* and *d*) which reduce the relative error between the two methods. Furthermore,

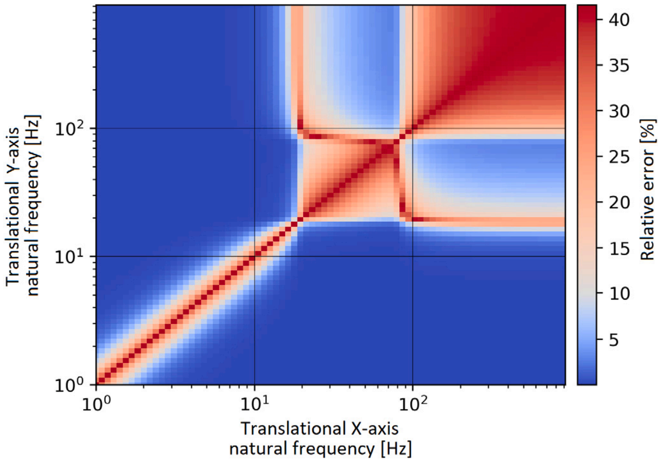

Fig. 8. Relative error map of standard vs proposed methods — Extreme response.

given the negligible contribution of one component, $n^+_{0,multi}$ closely approximates the dominant n^+_0 response:

$$\frac{s_{RMS,2}}{s_{RMS,1}} \approx 0 \Rightarrow n^+_{0,multi} \approx n^+_{0,1} \tag{48}$$

This results in a simplification of the ratio between the standard-computed damage and the multiaxial one (Eq. (47)), by considering the dominant response only (Eq. (48)):

$$\frac{\mathrm{FDmS}_{NB}}{\mathrm{FDS}_{std}} \approx \frac{n^+_{0,1}}{n^+_{0,1}} = 1 \tag{49}$$

2. Both components are equally participating in the multiaxial response at a given resonant frequency (Fig. 7-*a* and *c*). In that simple case study, it means that the n^+_0 of both components are similar:

$$s_{RMS,1} \approx s_{RMS,2} \Rightarrow n^+_{0,multi} \approx n^+_{0,1} \approx n^+_{0,2} \tag{50}$$

Since no component is negligible, the relative error between the two methods increase (Fig. 7-*a* and *c*) till reaching the maximum estimated relative error:

$$\frac{\mathrm{FDmS}_{NB}}{\mathrm{FDS}_{std}} \approx \frac{n^+_{0,1} \cdot 2^{\,b/2}}{n^+_{0,1} + n^+_{0,1}} = 2^{\,b/2\,-1} \tag{51}$$

In this situation, an *S-N* exponent $b = 8$ conducts to a maximal relative error ratio of 8, which is consistent with the simulation results (Fig. 7-*e*). In general and for such simple uncorrelated load cases, the maximal error ϵ may be estimated from the number of considered degrees of freedom n_{DOF}:

$$\max(\epsilon) = n_{DOF}^{b/2\,-1} \tag{52}$$

For instance, the maximum relative error in the case of a triaxial load would be $3^{b/2-1}$.

A similar trend can be observed in extreme responses when comparing the ERmS of enveloped uniaxial responses to the multiaxial one. In this particular case, the modal proximity increases the extreme response by a factor of $\sqrt{2}/2$. The estimated extreme response gradually converges towards the enveloped extreme response ERS_{std} (Eq. (21)) as they become farther apart (Fig. 8). This behavior mirrors that of the FDmS in the case when $b = 1$.

The damage increase caused by a multiaxial loading over sequentially-applied loads has been demonstrated in other experimental reviews [10,42,43] along with the impact of modal proximity [44]. Therefore, despite this numerical simulation being conducted on a reference MDOF structure, it provides results that are consistent with the actual behavior of structures.

4.2. *Biaxial loading analysis: the contribution of multiaxial S-N curve*

When a structure is subjected to both a translational and rotational load, the use of a pure translational or rotational uniaxial *S-N* curve may either overestimate or underestimate the damage depending on the contribution of each load. To address this concern, a multiaxial system-equivalent *S-N* curve can be introduced, along with the parameters b_{eq} and C_{eq} (Section 3.1.3).

The contribution of this multiaxial *S-N* curve is investigated during the following case study by introducing two uncorrelated translational and rotational loads:

$$\Phi_{\ddot{x}}(f) = \Phi_{\ddot{\theta}_x}(f) = \begin{cases} 1 & \text{if } f \in [20; 80] \text{ Hz} \\ 0 & \text{else.} \end{cases} \tag{53}$$

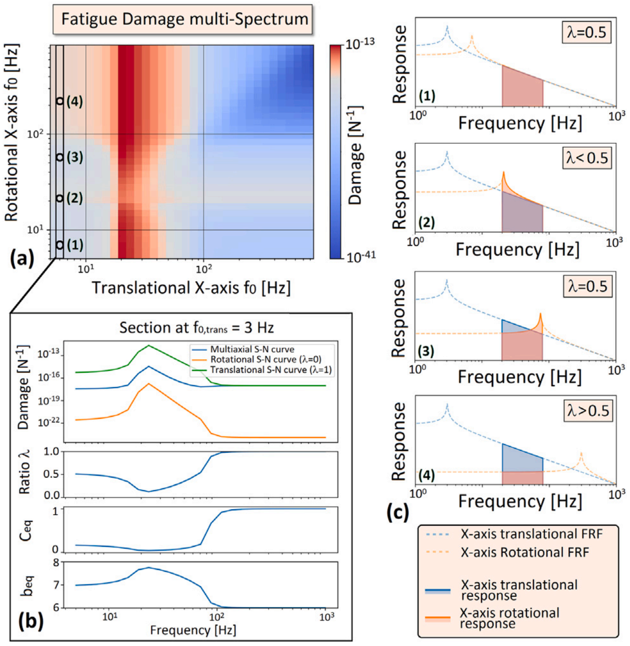

Fig. 9. Contribution of the multiaxial S-N curve on FDmS under biaxial translational/rotational loading.

Three FDmS are computed using either the pure rotational *S-N* curve (with standard values $b_r = 8$ and $C_r = 2$), the pure translational *S-N* curve (with values $b_t = 6$ and $C_t = 1$) or the multiaxial *S-N* curve. The damages resulting from these three multi-spectra are shown in a cross-section of the FDmS created at $f_{0,translation} = 3$ Hz, where multiaxial damage is greatly influenced by multiaxiality (Fig. 9-*b*). The FDmS using a system-equivalent multiaxial *S-N* curve is bounded by the FDmS using the translational curve and the one reliant on the rotational one. As stated in Section 3.1.3, its proximity to either of them depends on the multiaxiality coefficient λ (Fig. 9-*b*).

The participation of each component on the resultant response explains the behavior of λ (Fig. 9-*c*). When both resonant frequencies are below the excited frequency range, they have equal participation in the response, implying $\lambda \approx 0.5$ (case (1) on Fig. 9). Since the translational resonant frequency is fixed at $f_{0,translation} = 3$ Hz, the contribution of each load shifts as the rotational frequency varies. Specifically, the rotation gradually becomes the damage's dominant factor over translation, meaning $\lambda < 0.5$ (case (2) on Fig. 9). Finally, the increasing natural frequency of the rotational component will reduce its participation factor and, consequently, increase the relative influence of the translational load. Initially, this implies that the translational participation catches up with the rotational one before ultimately surpassing as rotation gradually becomes negligible (cases (3) and (4) on Fig. 9).

4.3. Correlated biaxial loading: the role of CSDs

The distinction between the standard sequential method and the proposed multiaxial procedure extends beyond the proximity of each DOF response alone. Multiple experiments have showcased the potential influence of the correlation between the components of multiaxial loads on structural damage [27–29,45]. This case study aims to highlight the FDmS's capability to account for correlations between axes. The assessment of load severity involves two correlated translational loads defined as follows:

$$\Phi_{\ddot{x}}(f) = \Phi_{\ddot{y}}(f) = \begin{cases} 1 & \text{if } \ f \in [20; 80] \text{ Hz} \\ 0 & \text{else.} \end{cases} \tag{54}$$

Various correlations between these components are studied with the help of a scalar criterion denoted as r_D (Eq. (55)). This criterion is defined as the frequency mean of the damage ratio between correlated and uncorrelated loads:

$$r_D = \frac{1}{\Delta f} \cdot \sum_{f_{min}}^{f_{max}} \frac{\text{FDmS}_{NB,\ correlated}}{\text{FDmS}_{NB,\ uncorrelated}} \tag{55}$$

This ratio is estimated for various phase-shifts with a 11.25° step and for several coherence levels with a 0.25 step. The findings are visualized using polar charts (Fig. 10) where the radial axis describes the coherence level and the angle depicts the phase-shift.

In this example, the biaxial load is represented by two translational accelerations along both axes X and Y. This can be viewed as two normal stresses applied to these axes from a material perspective. In that extend, the results presented in Fig. 10 align with the experimental findings of Papadopoulos, who demonstrated that two out-of-phase normal stresses are more damaging than an in-phase configuration [46].

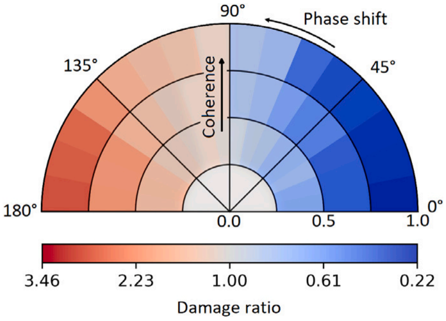

Fig. 10. Impact of cross-correlation on estimated damage.

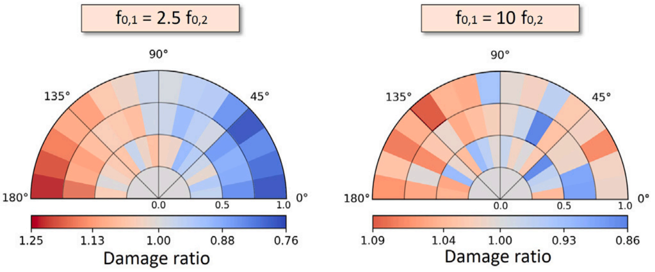

Fig. 11. Influence of modal proximity on cross-correlation severity.

Moreover, at a ±90° phase-shift, one signal reaches its peak while the other reaches zero, leading to an alternation of two loads applied successively on their respective axes. It means that this configuration is quite similar to the sequentially-applied uniaxial load case. As a result, the loads behave like two uncorrelated signals making the damage independent of the coherence level. This phenomenon, perceptible on Fig. 10, has also been experimentally observed by other works [27,28] in specimens exposed to flexion and torsion loads, suggesting its independence from the load configuration.

Another similarity with other studies available in the literature is the fast decrease in correlation severity as resonant frequencies become more distant (Fig. 11). In fact, the increasing distance between the frequencies on each axes reduces the amplitude of CSD terms (Eq. (6)), which narrows the gap between correlated and uncorrelated loads [44]. This statement is supported by the works of Preumont [31] and Vantadori et al. [47] which underscore that the gap between multiaxial and sequentially-applied loads also decrease. This supports the assertion made in Eq. (45): neglecting CSDs – and by extension cross-correlations or even multiaxiality itself – when natural frequencies are close enough can lead to significant errors. However, it may be acceptable when dealing with highly distant modes.

Therefore, the proposed FDmS formulation appears to offer a consistent depiction of multiaxial phenomena experimentally observed in real-life structures, even though it is a system-oriented procedure with no concern on the actual stress-state accuracy. It is the very objective of the proposed method to enable the characterization and comparison of various environments in terms of severity, either independently or in relation to any real-life structure and with the added capability of describing multiaxial phenomena.

The impact of CSDs on extreme response can also be analyzed using ERmS (Section 3.3) on various biaxial load configurations (Fig. 12). Despite the absence of any noticeable effect of correlation on biaxial linear accelerations, there is a significant contribution of CSDs involving angular accelerations, as emphasized by the coefficient matrix $\mathbf{Q_a}$ (Eq. (35)) and illustrated in Fig. 12-*a*. Since the impact of CSDs depends to the point's coordinates (x_0, y_0, z_0) used (Fig. 12-*b*), they are set equal to $(\sqrt{2}/2, \sqrt{2}/2, \sqrt{2}/2)$ in this example. As schematized in Fig. 12-*b*, whether the correlation has a increasing of decreasing effect on the resultant is also directly influenced by the direction of the axes.

4.4. Triaxial loading scenario

The preceding sections have illustrated how the proposed multiaxial procedure can effectively consider multiaxiality effects. This approach enables the characterization of correlated biaxial environments while maintaining a similar workflow to standard FDS and ERS methodologies.

In this section, the procedures are also applied to an uncorrelated triaxial translation load case to demonstrate their performance in a more complex configuration. This analysis requires the introduction of new illustrations to ease the comprehension of the results. In addition and for clarity purpose, the first triaxial study case relies on a load consisting of three uncorrelated PSD components defined by a broadband white noise signal in the frequency range of [1; 1000] Hz.

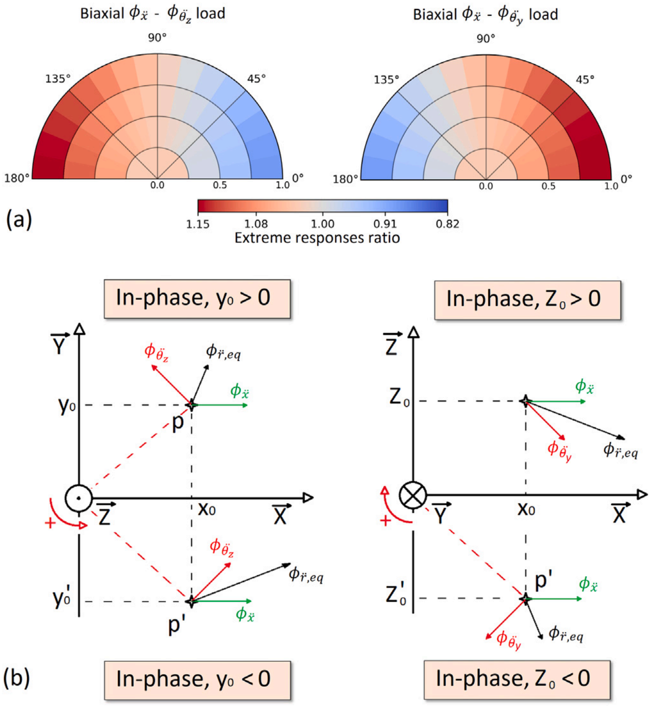

Fig. 12. Impact of correlation on biaxial extreme response depending on the loaded axes: extreme response ratio (a) and interpretation of the results (b).

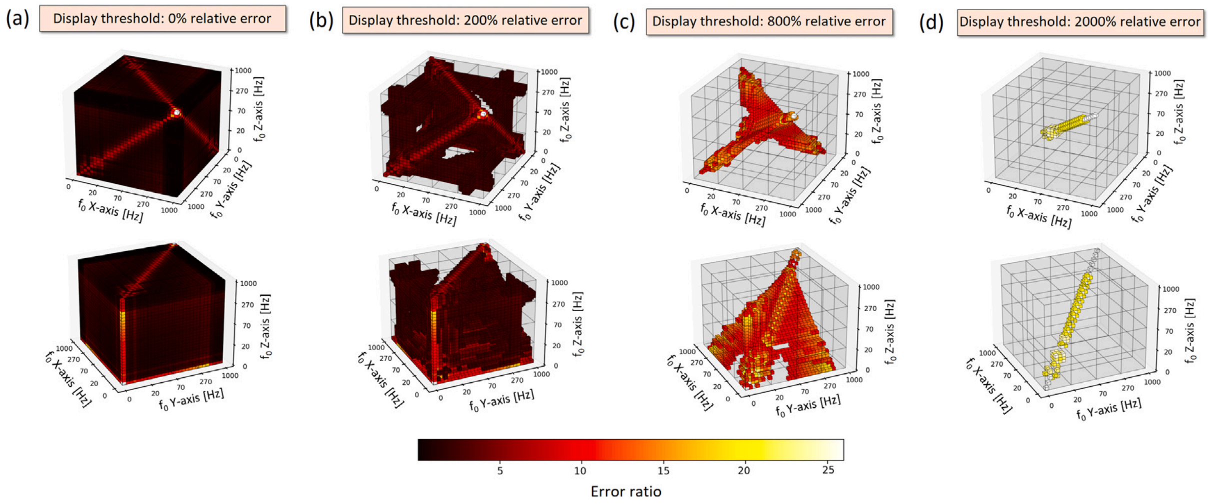

Fig. 13. FDmS illustration of a triaxial load.

Given that the numerical computation of tri-dimensional fatigue damage spectra require significantly more resources compared to uniaxial ones, the frequency resolution for this analysis is intentionally coarse. To elaborate, calculating FDmSs with n_f frequency steps per axis require a total of ${n_f}^{n_{DOF}}$ computational steps, where n_{DOF} represents the number of axes analyzed. As a result, the subsequent spectra are described using 20 logarithmically spaced frequency steps, ranging from 5 Hz to 1000 Hz, in contrast to the 90 steps for the previous biaxial analysis. The tri-dimensional FDmS representation takes the form of a filled volume (Fig. 13-*a*). To enhance clarity, a display threshold is introduced to conceal low damage ratio regions (Fig. 13-*b*, *c*, *d*).

The insights derived from the examination of biaxial loads are equally applicable to tri-axial loads. Notably, the most significant discrepancies between the standard, sequentially-applied loads and the multiaxial approach are observed along the diagonals of the volume's outer surfaces (Fig. 13-*a*). On these diagonals, the relative error remains consistently at 700% (equivalent to a ratio of 8 or $2^{b/2-1}$). Raising the display threshold highlights the cube's diagonal $f_{0,X} = f_{0,Y} = f_{0,Z}$. This is the location with the most substantial

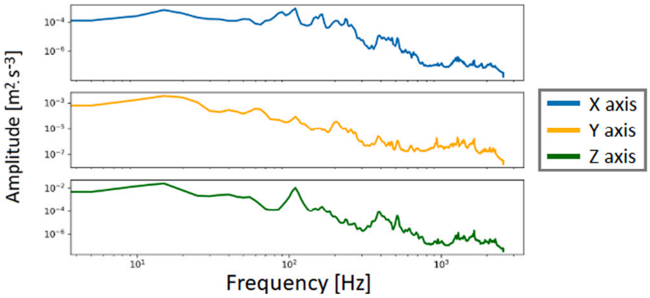

Fig. 14. PSDs of the recorded triaxial signal.

relative discrepancies between the two methods, with a constant 2600% error (equivalent to a ratio of 27, or $3^{b/2-1}$ as estimated by Eq. (52)). When it comes to extreme response, the maximal error between the ERmS and the ERS_{std} is $\sqrt{3}$.

While encountering a system subjected to three identical superimposed modal responses is highly improbable, the multiaxial approach estimates damage to be at least twice as significant as the standard method in nearly 80% of the computed volume (Fig. 13). This suggests that the conventional sequentially-applied load procedure may potentially underestimate damage in a significant portion of real-life structures. To a lesser extent, a similar conclusion can be drawn regarding the extreme response, which exceeds the standard method by at least 15% in almost 80% of the computed volume.

4.5. *Real-world load case analysis*

The numerical comparison between the proposed multiaxial method (Eq. (41)) and the standard sequentially-applied load approach (Eq. (16)) discussed previously was conducted on simulated loads. In this section, the load is defined by a real data-set recorded during a package trucking operation. This dataset consists of a 20-minute long signal sampled at 5.1 kHz, offering information on the X, Y and Z components of the triaxial environment (Fig. 14). These components respectively represents the travel direction as well as the longitudinal and vertical ones.

4.5.1. *Signal processing for procedure compatibility*

An almost-stationary and almost-Gaussian section of the full-length data-set has firstly been extracted to allow the use of specification development procedures. It is important to note that the three axes X, Y and Z must be processed as a unified dataset in order to preserve the cross-correlation information between the axial components. Consequently, the processing becomes a bit more complex and identifying signal segments where all axes exhibit simultaneous stationarity and Gaussian distribution characteristics can be a challenging task.

Even though numerous stationarity and normal tests are available to characterize signals [13], the selected process involves dividing the signal into 100 11.6 s windows and analyzing five key parameters: mean value, RMS value, auto-correlation, kurtosis and skew. These parameters are calculated using Python's *scipy.stats* module for kurtosis and skewness, and the *scipy.signal.correlate* function for auto-correlation. The analysis tracks the convergence of these parameters as windows are progressively added to characterize the signal's stationarity and conformity to a Gaussian distribution. The window length was arbitrarily set to 11.6 s as a compromise between high temporal resolution but noisy results and smooth outcomes with coarser temporal resolution in Fig. 15-*a*. It is noteworthy that this value has no impact on any other results whatsoever.

To clarify the process, the RMS value is initially calculated for the first 11.6-second window, followed by the RMS value for the combined first two windows, and so on, until the RMS value for the entire dataset is computed. Consequently, the Y-axis value corresponding to time t on Fig. 15-*a* matches with the value within the recorded time range of $[0, t]$. The properties of the entire signal are subsequently presented at $t = 1160$ s.

Despite this analysis focuses on the X component of the signal, the others are processed in a similar manner.

For this analysis, it is recalled that the auto-correlation (Eq. (1)) can be proven equal to the sum of each signal window auto-correlation. In the case of a perfectly stationary data-set, windows of equal duration should exhibit the same auto-correlation value. Consequently, there should be a linear relationship between the number of processed windows and the auto-correlation value. In this study, the auto-correlation value is computed using the *correlate* function from the *Numpy* module in Python.

The processing results indicate a zero-mean signal property and a convergence of the RMS value with minimal fluctuations (Fig. 15-*a*). In addition, there is a almost linear relationship between the auto-correlation and the number of processed windows ($R^2 = 0.993$ and p-value of 3.10^{-17}). These characteristics strongly suggest that the signal can be considered stationary [12,15]. This assertion is further substantiated by the Augmented Dickey–Fuller test results: with an estimated p-value of 2.10^{-22} and a statistic of -12.1, the non-stationary hypothesis can be rejected at a 99% confidence.

Although the data-set is not perfectly Gaussian (Fig. 15-*b*), it can still be considered close enough to meet the requirements for comparison between the standard and multiaxial procedures.

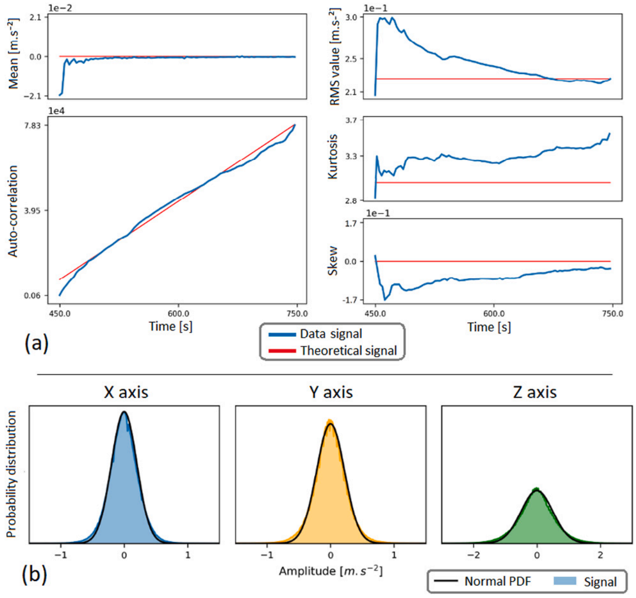

Fig. 15. Statistical properties of the recorded signal.

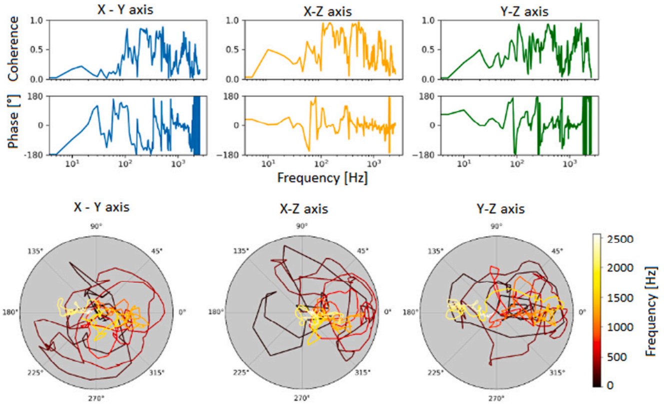

Fig. 16. CSDs of the recorded triaxial signal.

A noteworthy point relates to the CSDs derived from the spectral processing of the recorded signal (Fig. 16). These CSDs offer insights into the cross-correlations between multiaxial load components [13,14]. Their illustration clearly demonstrates substantial variability in the CSD values across frequencies.

With an average coherence of approximately 0.4 for each component and a peak value of 0.9, it becomes evident that neglecting cross-correlations in the context of multiaxial fatigue analysis in real-world scenarios may not always be justified. This underscores a potential limitation in the assumptions commonly made by standard procedures.

4.5.2. Sample damage assessment

To enhance clarity, the triaxial load is initially divided into three biaxial loads, as depicted in Fig. 17-*a*. This decomposition, while resulting in an underestimation of multiaxial damage due to the omission of certain correlations, simplifies the representation and analysis of the results without affecting the overall interpretation. A comprehensive discussion of the complete tri-axis load will follow.

When comparing the damage estimations derived from the sequential procedure and its multiaxial counterpart, significant inaccuracies become noticeable (Fig. 17-*a*). This suggests that the true impact of the trucking environment on the monitored package was likely more severe than the initial estimate provided by the sequential procedure.

Furthermore, the impact of cross-correlations between the environmental components can be evaluated by either incorporating or omitting the CSDs within the proposed multiaxial procedure. In this specific case study, it is observed that cross-correlations

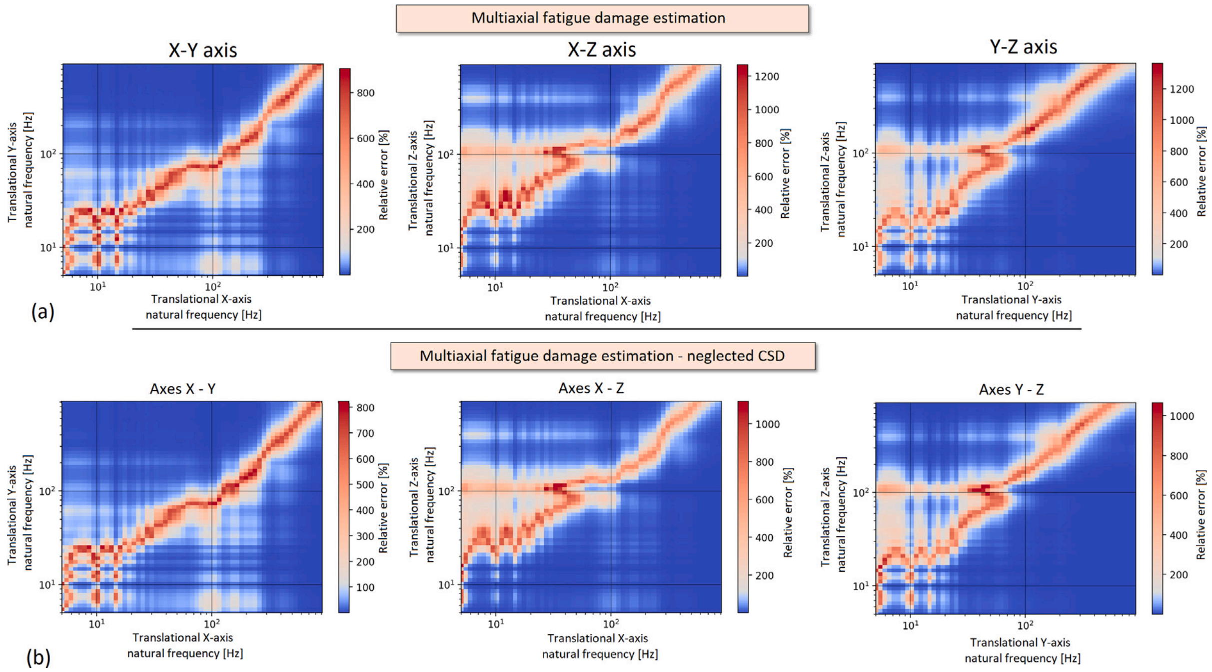

Fig. 17. Relative error map between standard and proposed methods — FDmS of a real load case.

between the $X-$ and $Y-$ components account for 5% of the total damage, whereas the X-Z and Y-Z cross-correlations contribute to 10% and 20% respectively (Fig. 17-*b*).

The contribution of these CSDs on the fatigue damage assessment suggests that neglecting cross-correlations may likely cause damage under-estimation even in common real-life loads such as road transportation.

When evaluating ERmS, smaller discrepancies are observed, peaking at only 50%. However, these errors are more widely spread across the entire range of resonant frequencies (Fig. 18). It is worth noting that no analysis was conducted to assess the influence of cross-correlations on ERmS. This is due to the fact that the time series used in this study case only refer to triaxial linear accelerations, and their cross-correlations do not impact the extreme response of the structure (Section 3.3).

The analysis of the complete triaxial environment yields comparable outcomes, with CSDs accounting for up to 20% of the total estimated damage (Fig. 19). To enhance the clarity of the FDmS for the triaxial load, a display threshold of 1000% has been set to conceal the FDmS areas where the damage ratio between the two methods is less than 11.

5. Conclusion

The proposed spectral methods for characterizing multiaxial vibrations are built upon the uniaxial procedures of the standard AFNOR NF X50-144. They generalize the widely-used FDS and ERS into a fatigue damage multi-spectrum (FDmS) and extreme response multi-spectrum (ERmS) respectively. These spectra are specifically designed to assess the severity of multiaxial environments, thanks to the implementation of an equivalent stress response PSD and a system-equivalent multiaxial *S-N* curve. These components are derived from the Lemaitre equivalent stress PSD and the modified Wöhler curve method, respectively.

The proposed method for generating multiaxial fatigue damage spectra, including bi- and tri-dimensional versions, demonstrates superior performance compared to standard procedures in numerical case studies. This improvement arises from its capacity to account for multiaxial influences such as structural modal proximity and environmental cross-correlations. Additionally, the assessment of fatigue damage and extreme responses using the proposed FDmS and ERmS methods aligns with existing literature findings.

A key result of this study, based on the parameters used, shows that when axial RMS stress responses contribute equally, there is a significant increase in fatigue damage. This means that even with widely-spaced natural frequencies, multiaxial loads can still impact structures while being overlooked by uniaxial procedures. This observation challenges the validity of empirical rules in some industries that ignore multiaxial effects by relying on modal proximity ratio thresholds.

In addition, The proposed multiaxial procedure highlights the limitations of conventional methods, which underestimate multiaxial damage by ignoring correlations and cross-axis interactions. This was demonstrated through virtual loads and real-world data, showing that correlations can contribute up to 20% of estimated fatigue damage (on the basis of the parameters used in that example). Neglecting load's cross-correlations may therefore be unjustified in some cases.

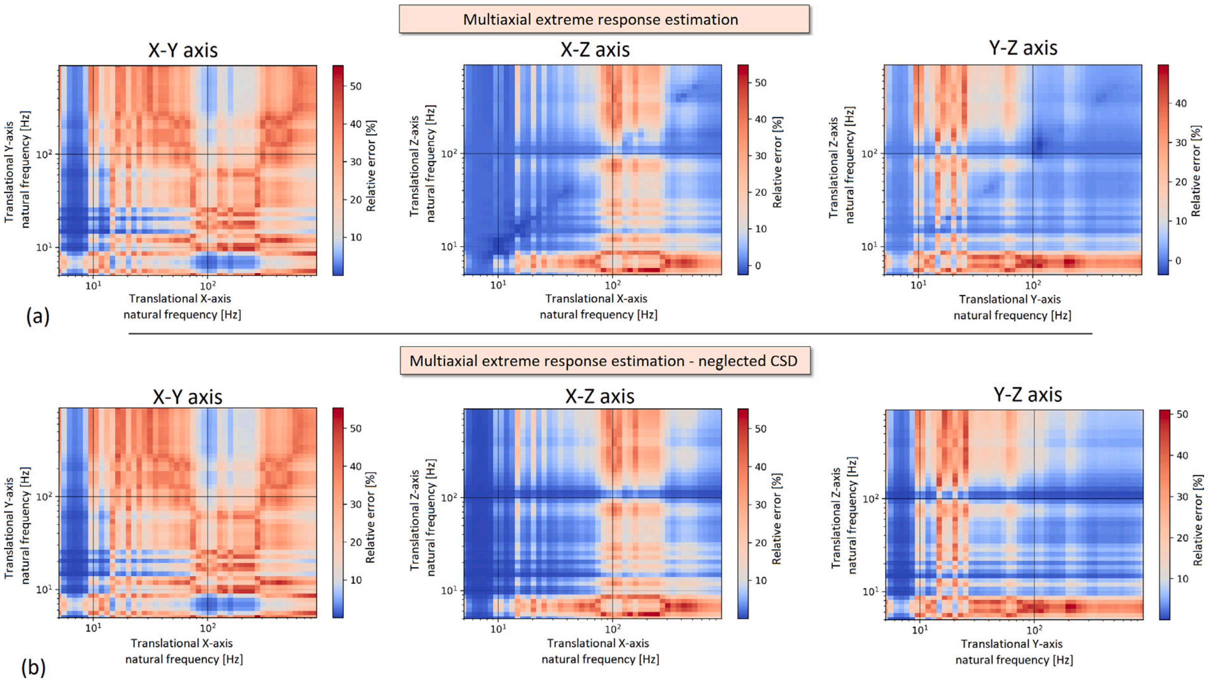

Fig. 18. Relative error map between standard and proposed methods — ERmS of a real load case.

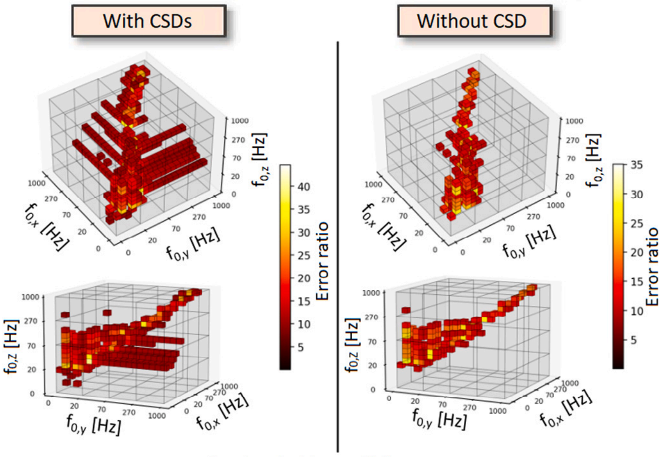

Display threshold: 1000% damage error

Fig. 19. Impact of cross-correlation on real-world triaxial environment.

In conclusion, accurately assessing damage caused by multiaxial loads necessitates procedures capable of accounting for the multiaxial nature of the environment and the cross-correlations among its components. Otherwise, neglecting these factors may result in significant underestimations of the structure's response.

CRediT authorship contribution statement

M. Aimé: Writing – original draft, Methodology, Investigation. **A. Banvillet:** Resources, Funding acquisition, Conceptualization. **L. Khalij:** Writing – review & editing, Formal analysis. **E. Pagnacco:** Formal analysis. **E. Chatelet:** Validation, Resources. **R. Dufour:** Supervision, Resources.

Declaration of competing interest

The authors declare that they have no known competing financial interests or personal relationships that could have appeared to influence the work reported in this paper.

Data availability

The authors do not have permission to share data.

Acknowledgments

The authors express their gratitude to the French Alternative Energies and Atomic Energy Commission (CEA), which provided financial support for this research.

References

[1] C. Braccesi, F. Cianetti, G. Lori, Random multiaxial fatigue: A comparative analysis among selected frequency and time domain fatigue evaluation methods, Int. J. Fatigue 74 (2015) 107–118.
[2] D. Benasciutti, R. Tovo, Frequency-based analysis of random fatigue loads: Models, hypotheses, reality, Mater.wiss. Werkst.tech. 49 (2018) 345–367.
[3] M. Muñiz-Calvente, A. Álvarez Vázquez, F. Pelayo, M. Aenlle, N. García-Fernández, M. Lamela-Rey, A comparative review of time- and frequency-domain methods for fatigue damage assessment, Int. J. Fatigue 163 (2022).
[4] AFNOR, NF X50-144: Demonstration of resistance to environmental conditions, 2014.
[5] F. Xu, K. Ahlin, B. Wang, Optimization of damage equivalent accelerated test spectrum derivation using multiple non-gaussian vibration data, J. Sens. (2021).
[6] I.A. Coutinho, J. Landre, Enhanced tailored durability test specification for multiaxial dynamically excited structures attached to a single input base under off-road loading environment, Eng. Struct. 219 (2020).
[7] M. Decker, Vibration fatigue analysis using response spectra, Int. J. Fatigue 148 (2021).
[8] O. Touzanov, M.J. Guers, Application of the fatigue damage spectrum to accelerated vibration testing, J. Acoust. Soc. Am. (2019).
[9] N. Nath, G. Aglietti, Study the effect of tri-axis vibration testing over single-axis vibration testing on a satellite, 2022, pp. 1–10.
[10] E. Proner, E. Mucchi, R. Tovo, Fatigue behaviour assessment and time to failure predictions under multi-axis vibration environments, Mech. Syst. Signal Process. (2023) Preprint submitted to.
[11] U. Musella, M.A. Blanco, D. Mastrodicasa, G. Monco, Combining test and simulation to tackle the challenges derived from boundary conditions mismatches in environmental testing, in: Sensors and Instrumentation, Aircraft/Aerospace, Energy Harvesting & Dynamic Environments Testing, Vol. 7, 2020, pp. 259–269.
[12] J. Slavič, M. Mršnik, M. Česnik, J. Javh, M. Boltežar, Chapter 2 - signal processing, in: Vibration Fatigue by Spectral Methods, Elsevier, 2021, pp. 51–74.
[13] J. Bendat, A. Piersol, Random Data: Analysis and Measurement Procedures, in: Wiley Series in Probability and Statistics, 2010.
[14] J. Wijker, Random Vibration in Spacecraft Structures Design, Springer, 2009.
[15] C. Lalanne, Mechanical Vibration and Shock Analysis, Hermès, 1999.
[16] S.O. Rice, Mathematical analysis of random noise, Bell Syst. Tech. J. (1954).
[17] O. Basquin, The exponential law of endurence tests, Am. Soc. Test. Mater. (1910).
[18] A. Zorman, J. Slavič, M. Boltežar, Vibration fatigue by spectral methods—a review with open-source support, Mech. Syst. Signal Process. 190 (2023).
[19] I. Rychlik, On the 'narrow-band' approximation for expected fatigue damage, Probab. Eng. Mech. 93 (1993).
[20] M. Miner, Cumulative damage in fatigue, J. Appl. Mech. 67 (1945) 159–164.
[21] K. Hectors, W. De Waele, Cumulative damage and life prediction models for high-cycle fatigue of metals: A review, Metals (2021).
[22] A. Fatemi, L. Yang, Cumulative fatigue damage and life prediction theories: a survey of the state of the art for homogeneous materials, Int. J. Fatigue 20 (1998) 9–34.
[23] US Department of Defense, MIL-STD-810: Environnemental engineering considerations and laboratory tests, 2019.
[24] NAVMAT, P-9492: Navy manufacturing screening program, 1979.
[25] E. Habtour, G. Drake, Improved Reliability Testing with Multiaxial Electrodynamics Vibration, US Army Materiel Systems Analysis Activity, 2010.
[26] A. Almamoori, Y. Alizadeh, A novel approach to multiaxial fatigue life prediction using the critical plane and phase difference angle, Eng. Fail. Anal. 154 (2023).
[27] Z. Luo, C. Zhou, X. Fan, Y. Wang, G. He, H. Chen, The influence of load correlation on vibration fatigue damage of symmetrical notched cantilever beam structures, Fatigue Fract. Eng. Mater. Struct. 46 (2023).
[28] Z. Luo, S. Vantadori, Carpinteri, Vibration fatigue analysis of circumferentially notched specimens under coupled multiaxial random vibration environments, Fatigue Fract. Eng. Mater. Struct. 44 (2021) 2412–2428.
[29] F. Frendo, L. Bertini, Fatigue resistance of pipe-to-plate welded joint under in-phase and out-of-phase combined bending and torsion, Int. J. Fatigue 79 (2015) 46–53.
[30] J. Papuga, M. Nesládek, J. Jurenka, Differences in the response to in-phase and out-of-phase multiaxial high-cycle fatigue loading, Frattura Integrità Strutt. (2019).
[31] A. Preumont, Random Vibration and Spectral Analysis, Springer Science, 1994.
[32] X. Pitoiset, F. Preumont, Spectral methods for multiaxial random fatigue analysis of metallic structures, Int. J. Fatigue 22 (2000) 541–550.
[33] D. Benasciutti, Some analytical expressions to measure the accuracy of the Equivalent Von Mises Stress in vibration multiaxial fatigue, J. Sound Vib. 333 (2014) 4326–4340.
[34] M. Mrsnik, J. Slavic, M. Boltezar, Multiaxial vibration fatigue - a theoretical and experimental comparison, Mech. Syst. Signal Process. 76 (2016) 409–423.
[35] D. Benasciutti, F. Sherratt, A. Cristofori, Recent developments in frequency domain multi-axial fatigue analysis, Int. J. Fatigue 91 (2016) 397–413.
[36] A. Nieslony, A critical analysis of the mises stress criterion used in frequency domain fatigue life prediction, Frattura Integrità Strutt. 38 (2016) 177–183.
[37] J. Lemaitre, R. Desmorat, Engineering Damage Mechanics, Springer, 2005.
[38] J. Ge, Y. Sun, S. Zhou, Fatigue life estimation under multiaxial random loading by means of the Equivalent Lemaitre stress and multiaxial S–N curve methods, Int. J. Fatigue 79 (2015) 65–74.
[39] L. Susmel, P. Lazzarin, A bi-parametric Wöhler curve for high cycle multiaxial fatigue assessment, Fatigue Fract. Eng. Mater. Struct. 25 (2001) 63–78.
[40] B. Liu, X. Yan, A modified method of Von Mises stress-based MWCM for fatigue-life prediction under fully-reversed axial - torsion proportional loads, Mater. Technol. 53 (2018) 115–121, 1.

[41] L. Zou, D. Zeng, S. He, L. Lu, On the combination of a critical plane-based multiaxial fatigue criterion with the critical distance theory for predicting the fretting fatigue strength of press-fitted axles, Int. J. Fatigue 183 (2024).
[42] N. Nath, G.S. Aglietti, Study the effect of tri-axis vibration testing over single-axis vibration testing on a satellite, in: 2022 IEEE Aerospace Conference, AERO, 2022, pp. 1–10.
[43] R. Reza Kashyzadeh, Effects of axial and multiaxial variable amplitude loading conditions on the fatigue life assessment of automotive steering knuckle, J. Fail. Anal. Prev. 20 (2020) 455–463.
[44] I. Elishakoff, Normal-Mode Approach in Random Vibrations, Springer International Publishing, 2020, pp. 1–35.
[45] A. Cernescu, R. Pullin, New research findings on non-proportional low cycle fatigue, in: MATEC Web of Conferences, 2019.
[46] I. Papadopoulos, A high-cycle fatigue criterion applied in biaxial and triaxial out-of-phase stress conditions, Fatigue Fract. Eng. Mater. Struct. 18 (1995) 79–97.
[47] S. Vantadori, A. Carpinteri, G. Fortese, Influence of random fatigue loading non-proportionality on damage, Theor. Appl. Fract. Mech. 96 (2018) 56–63.